Lab on a Chip



PAPER

View Article Online



Cite this: DOI: 10.1039/d0lc00969e

Rapid isolation of circulating cancer associated fibroblasts by acoustic microstreaming for assessing metastatic propensity of breast cancer patients†

Ruoyu Jiang, ¹ Sudhanshu Agrawal, ^b Mohammad Aghaamoo, ^a Ritesh Parajuli, ^c Anshu Agrawal ^b and Abraham P. Lee ¹ **ad

We demonstrate a label free and high-throughput microbubble-based acoustic microstreaming technique to isolate rare circulating cells such as circulating cancer associated fibroblasts (cCAFs) in addition to circulating tumor cells (CTCs) and immune cells (*i.e.* leukocytes) from clinically diagnosed patients with a capture efficiency of 94% while preserving cell functional integrity within 8 minutes. The microfluidic device is self-pumping and was optimized to increase flow rate and achieve near perfect capturing of rare cells enabled by having a trapping capacity above the acoustic vortex saturation concentration threshold. Our approach enables rapid isolation of CTCs, cCAFs and their associated clusters from blood samples of cancer patients at different stages. By examining the combined role of cCAFs and CTCs in early cancer onset and metastasis progression, the device accurately diagnoses both cancer and the metastatic propensity of breast cancer patients. This was confirmed by flow cytometry where we observed that metastatic breast cancer blood samples had significantly higher percentage of exhausted CD8⁺ T cells expressing programmed cell death protein 1 (PD1), higher number of CD4⁺ T regulatory cells and T helper cells. We show for the first time that our lateral cavity acoustic transducers (LCATs)-based approach can thus be developed into a metastatic propensity assay for clinical usage by elucidating cancer immunological responses and the complex relationships between CTCs and its companion tumor microenvironment.

Received 24th September 2020, Accepted 4th December 2020

DOI: 10.1039/d0lc00969e

rsc.li/loc

Introduction

Metastasis is the leading cause of death for cancer as patients with metastasis have a higher than 70% death rate while nonmetastatic locoregional cancer patients have a higher than 85% five-year survival rate. Although a small percentage of women (5–10%) were diagnosed with breast cancer at a later metastasized stage, 30% of women diagnosed at an early nonmetastatic stage will eventually develop into the metastatic stage. This provides a critical window of opportunity for early diagnosis. Circulating tumor cells (CTCs) are actively shed off from primary and metastatic tumor sites into the bloodstream and a small fraction of them possess

The analysis of CTCs has evolved from simple enumeration to functional profiling of enzyme secretion, intracellular proteins, and genome sequencing to gain insights of molecular regulation and cellular heterogeneities involved with cancer invasiveness and immune system deficiency. However, cellular changes occurring within the tumor microenvironment termed 'pre-metastatic niche' induce various signaling events that are conductive to the CTC dissemination and formation of metastatic lesions long before tumor cells arrive, suggesting that a collective effort to move beyond measurements of CTCs is essential toward better understanding of cooperative interactions between CTCs and the tumor microenvironment and their roles in metastatic process. 2,3,11-13

Cancer associated fibroblasts (CAFs) are major components of tumor microenvironment and comprise majority of stromal cells. CAFs strongly modulate disease

the ability to colonize distant organs and form metastatic lesions. CTCs have been extensively used as liquid biopsy biomarkers to diagnose cancer occurrence and its phenotypic and genetic information are often used to understand tumor initiation, progression, and metastasis.⁴⁻⁶

^a Biomedical Engineering, University of California, Irvine, CA 92697, USA. E-mail: aplee@uci.edu

b Department of Medicine, Division of Basic and Clinical Immunology, University of California, Irvine, CA 92697, USA

^c Department of Medicine, Division of Hematology Oncology, University of California, Irvine, CA 92697, USA

^d Mechanical and Aerospace Engineering, University of California, Irvine, CA

 $[\]dagger$ Electronic supplementary information (ESI) available. See DOI: 10.1039/d0lc00969e

Paper Lab on a Chip

progression and immune system responses and produce growth factors such as hepatocyte growth factor and TGFB that are crucial for extracellular matrix (ECM) remodeling and tumor growth. 14-17 CAFs are traditionally identified within primary and metastatic tumor regions and can be isolated from digestion of patients' tumor tissues. Recent mouse models have first shown that the stromal components of the tumor microenvironment such as CAFs are also shed off along with CTCs and immune cells to the peripheral blood circulation and signal reciprocal communications with cancer cells for tumor metastasis. 4,18 The discovery of noncancer, non-immune cells were later being isolated in association with CTCs and identified as circulating CAFs (cCAFs) from human cancer patient blood. 4,19 Interestingly, cCAFs were mostly present in patients with metastatic breast cancer but not in blood from early stages of cancer patients, while CTCs were detected in all stages of cancer. 4,19,20 In addition, circulating immune cells such as cytotoxic T cells, regulatory T cells and macrophages are important indicators of immune suppression resulted from CTC dissemination and tumor growth.^{8,13,21} A productive communication between CTCs and their environment likely results in a successful disguise for CTCs to escape immune surveillance, ultimately leading to metastatic seeding at distant organs.3,11 A simultaneous capture of multiple types of cells represents an important step toward unmasking the dynamic relationships between tumor cells microenvironment in relation to immunological responses.

The standard laboratory method to capture and analyze CTCs is based on CellSearch® system approved by The Food and Drug Administration (FDA). Cancer cells are magnetically isolated based on epithelial cell adhesion molecule (EpCAM) surface markers expressed predominantly on CTCs and the capture efficiency is heavily influenced by the EpCAM expression level. As a result, the system has low capture efficiency of CTCs that are undergoing epithelial to mesenchymal transition (EMT), and the CTC tests based on surface biomarker expression have been limited due to the low sensitivity and specificity of the detection methods.²²⁻²⁴ An erroneous diagnosis may mistakenly expose early stage cancer patients to aggressive treatments or leave metastatic patients undiagnosed. Consequently, diagnosis based on CTC counts has not offered significant improvements in terms of overall survival (OS) for metastatic cancer patients, demanding a need to search for companion biomarkers along with CTCs. 7,25,26 Moreover, in the case of single cell RNA sequencing, cellular secretion analysis and cancer cell culturing, the system applies fixation steps that disrupt cellular viability and render analytic steps that require live cells unfeasible. Recent advances in microfluidic technologies have offered alternative yet robust label free approaches to capture CTCs from peripheral blood based on physical differences and electrical membrane properties, including inertial microfluidics, 27-30 surface acoustic wave (SAW), 31-33 optical force34 and dielectrophoresis.35 High throughput microfluidic platforms are promising and can achieve high

cell capture efficiency and cell viability. However, these microfluidic systems often rely on external syringe pumping systems to flow blood samples through the devices, decreasing the overall portability and increasing usage of laboratory space. A self-pumping microfluidic system is most ideal for clinicians to obtain results at the most optimal time near the location of the patients.36

To overcome these challenges, we have previously established a label-free platform for bead and cell separation from ultrasonicrange acoustic energy while preserving cell integrity and viability. 37-39 The system pumps sample solution without external syringe pumps solely through the vibration of the air-liquid interfaces powered by piezoelectric transducers (PZT). The acoustic microstreaming patterns generated from air-liquid interface vibrations allow simultaneous fluid pumping and particle trapping. In this study, our device is modified to include four 101-pair of lateral cavity acoustic transducers (LCATs) with one shared inlet and two outlets (Fig. 1a and b). The bulk flow was intensified to enable the high-density LCATs to not only draw fluid in four directions simultaneously to facilitate blood sample pumping, but also prevent rare cell loss caused by cell-cell collision from high number of blood cells, which can have the trapped rare cells escape from the vortex (Fig. 1c). Using this design, we can isolate CTCs, cCAFs and circulating immune cells within 8 minutes from red blood cell (RBC) lysed 7.5 mL of breast cancer patient blood while achieving 94% of capture efficiency without compromising the viability of cells, preserving the natural state of rare cells and enabling clinicians to better understand cancer metastasis and identify novel therapeutic regimes. We further examined diagnostic performance of CTCs and cCAFs for nonmetastatic cancer and metastatic cancer prediction and conducted flow cytometric analysis of circulating T cells' immune suppression responses in relation to breast cancer progression.

Materials and methods

Microfluidic device fabrication

In this study, devices were fabricated using standard soft lithography processes on a 4 inch silicon wafer. Channel layer was spin coated with SU-8 2075 (MicroChem, USA) at speed of 500 rpm for 10 seconds and then followed by 2100 rpm for 30 seconds for 100 µm heights. Devices were soft baked at 65 °C for 5 minutes and 95 °C for 15 minutes and cooled for 3 minutes. They were exposed and patterned by ultraviolet for 22 seconds with chrome mask (FrontRange, USA). The wafer was then post exposure baked at 65 °C for 5 minutes and 95 °C for 10 minutes. A sonicator was used for 45 seconds and handshook for 3 minutes to remove unexposed photoresist from the wafer. Devices were then cure baked at 220 °C for 3 minutes. LCATs were then made with the polymer polydimethylsiloxane (PDMS) and Sylgard 184 Silicone Elastomer Curing Agent (Dow Corning, USA) at 11.5:1 ratio. After sitting at room temperature overnight, the PDMS channel was peeled from the mold and bonded to the glass. Before bonding, the PDMS channel and glass were treated with oxygen plasma and placed on a hotplate at 90 °C overnight.

Fig. 1 LCATs design principle. a) Large cells are trapped in bubble based acoustic microstreaming while smaller cells are released. b) Camera photo demonstrating LCATs with respect to the scale of one quarter coin. c) LCATs capture large cells and release small cells. Cells can be further released by washing with $1\times$ PBS. Scale bar: $100 \mu m$.

Separation design of LCATs

Following previous works, we describe the LCATs working principle for separation as follows: the symmetry of dead end side channels enables the assumption that the bulk flow can be divided evenly through both narrow gaps $(D_{\rm gap})$ near the air–liquid interfaces. ^{40,42,43} The total volumetric flow rate through half the cross-sectional area $(V_{\rm main})$ of the microchannel is:

$$V_{\text{main}} = \left(\frac{W}{2}\right) \times H \times U_{\text{b}} \tag{1}$$

W denotes the width of the microfluidic channel, H is the height of the channel, and $U_{\rm b}$ is the average velocity of the bulk flow. The total volumetric flow rate through a narrow gap at the air/liquid interface ($V_{\rm gap}$) is:

$$V_{\rm gap} = U_{\rm s} \times D_{\rm gap} \times H \tag{2}$$

 $U_{\rm s}$ is the second order streaming flow velocity near the airliquid interface. The total volumetric flow rate through the main channel ($V_{\rm main}$) will also equal the volumetric flow rate through the narrow gap ($V_{\rm gap}$) based on the continuity theory.

 $D_{\rm gap}$ can be described as:

$$D_{\rm gap} = \left(\frac{W}{2}\right) \times \left(\frac{U_{\rm b}}{U_{\rm s}}\right) \tag{3}$$

Calculation of acoustic microstreaming cell capture efficiency

The calculation to determine acoustic microstreaming saturation and rare cell capture efficiency is described as follows:

$$\frac{\text{(The total number of injected cells - The total number of lost cells)}}{\text{(The total number of injected cells)}} \times 100\%$$

Rare cell isolation

After the patient's whole blood was treated with RBC lysis buffer, we added 500 μ L of 1× PBS with 2% FBS to cell pellets and then transferred the solution into LCATs chips (width = 750 μ m) for processing. LCATs chip was placed on top of a piezoelectric transducer (Steiner and Martins, Inc., USA) with ultrasound gel applied between chip glass and surface of the piezoelectric transducer (Fig. S1†). During rare cell isolation, trapped cells were then washed with 1× PBS with 2% FBS

Paper

twice to remove residual RBCs. After washing, we manually pushed the cells remaining in the LCATs channels with 1× PBS with 2% FBS to avoid cell loss. We repeated this procedure until 99% of cells were pushed out of the LCATs channels.

Cell line experiment and preparation

Normal human lung fibroblasts (NHLF) were purchased from Lonza and were cultured with DMEM (Corning, USA) containing 10% (vol/vol) FBS (Thermo Fisher Scientific, USA). Cells were cultured in an incubator at a temperature of 37 °C and 5% CO2 level. Before each experiment, cells were detached from the surface of culture flasks with 0.05% trypsin (Corning, USA) and DMEM. Suspended cells were then centrifuged at 300 g for 3 minutes. To label fibroblasts with red cell tracker dye, cell pellets were incubated with red cell tracker dye at 500 µL with concentration of 7.5 µM at room temperature. Cells were washed and centrifuged at 300 g for 3 minutes and resuspended into 1× PBS with 2% FBS.

Patient blood processing, immunofluorescence staining, and image acquisition

Females with breast cancer were consented to a UCI IRB approved clinical protocol permitting blood collection for cCAFs under Clinical Trial UCI-17-43. and Immunostaining of EpCAM, fibroblast activated protein (FAP) and immune cell marker CD45 as well as nucleus staining of 4',6-diamidino-2-phenylindole (DAPI) were used to identify collected cells. CTCs were identified as EpCAM⁺/FAP⁻/CD45⁻/ DAPI⁺; cCAFs were identified as EpCAM⁻/FAP⁺/CD45⁻/DAPI⁺; white blood cells (WBCs) were identified as EpCAM⁻/FAP⁻/ CD45⁺/DAPI⁺. Whole blood samples were collected in 7.5 mL ethylenediaminetetraacetic acid (EDTA) tubes and used within 24 hours after collection. Red blood cells in the collected samples were then lysed by a 10 minutes treatment of RBC lysis buffer, followed by centrifugation at 350 g. After removing the supernatant, CTCs, cCAFs and WBCs were collected and resuspended in 500 µL of 1× PBS solution with 2% FBS. The mixture was then processed through the microfluidic device. The isolated cells were collected and concentrated via centrifugation to 100 immunofluorescence staining.

To perform staining, cells were blocked with 10 µL of human TruStain FcX (Biolegend, USA) for 15 minutes to block nonspecific binding sites on Fc receptors. For CTCs immunostaining, 5 µL of Alexa Fluor 488-labeled anti-human EpCAM (Biolegend, USA) and 5 μL Alexa Fluor 594-labeled anti-CD45 (Thermo Fisher Scientific, USA) were added and cells were incubated on ice in dark for 20 minutes. For cCAFs immunostaining, 1 µL of rabbit anti-human FAP (Thermo Fisher Scientific, USA) and 5 µL Alexa Fluor 594-labeled anti-CD45 (Thermo Fisher Scientific, USA) were added and cells were incubated on ice in dark for 20 minutes. Cells were then washed and 1 µL of 100-fold diluted secondary goat antirabbit (Sigma-Aldrich, USA) was added to 100 µL of cell

pellets and cells were incubated on ice in dark for 20 minutes. Cell pellets were then stained with DAPI (Thermo Fisher Scientific, USA). Cells were imaged using IX51 fluorescence microscopy (Olympus, Japan) and a SLR camera. The images were processed and analyzed using ImageJ. The 2D projection of cells was then calculated by measuring the contour length of the resulting binary pixel image locations using ImageJ JFilament 2D.

Flow cytometry immuno-phenotyping

Peripheral blood mononuclear cells (PBMCs) were isolated from blood (15 to 20 ml) of metastatic breast cancer and nonmetastatic locoregional breast cancer patients separation medium density lymphocyte gradient centrifugation. Following fixable viability staining as per manufacturer's protocol, cells were washed and stained with appropriate antibodies and FMO controls. Cells were washed with a staining buffer (PBS +2% FBS) or fixed in 2% PFA and analyzed. Flow cytometry was performed using FACSCelesta (Becton-Dickinson, San Jose, CA). Ten thousand cells were acquired and analyzed using Flowjo software (Treestar, Ashton, OR). Percent positive cells and MFI were determined.

Results

Lateral cavity acoustic transducers (LCATs) for selective trapping and pumping

LCATs rely on oscillation of trapped microbubbles in lateral slanted dead end side channels to generate a first order oscillatory flow at the air-liquid interface. 40-43 The first order oscillatory flow induces a second order streaming flow that consists of an open microstreaming flow and a close looped microstreaming vortex (Fig. 1 and S2†). The dead end side channels were designed to have a 15° slanted angle so that the open microstreaming generates a bulk flow that pumps through the main channel. In the flow region between the close looped microstreaming vortex and air-liquid interface, there is a narrow gap (D_{gap}) that is controlled by voltage and it sets a size threshold for particles to pass through: higher voltage leads to larger $D_{\rm gap}$ and lower voltage leads to smaller $D_{\rm gap}$ (as defined in Materials and methods). Particles with radii smaller than the $D_{\rm gap}$ travel forward with the bulk flow while larger particles are trapped within close looped acoustic microstreaming vortices. 29-32

To characterize and validate our platform's pumping and cell trapping efficiency, we first used an LCATs with 200 pairs of dead end side channels to determine the acoustic microstreaming saturation and capture efficiency. In previous work, whole blood was pumped by an external syringe pump at a flow rate of 25 μL min⁻¹ and the acoustic microstreaming acted solely as cell traps to achieve maximum cell capture.³⁷ Nevertheless, external flow potentially hinders microbubble stability and limits trapping performance over time for large volume of blood samples such as 7.5 mL (Fig. S3 and S4†). The primary strength of the LCATs technology is the ability to both pump the fluid sample and trap cells without the

need for external syringe pumps. We measured the cell capture efficiency by injecting human fibroblasts at known concentrations into devices (width = 500 µm) and evaluated the trapping efficiency as a function of the number of injected cells (Fig. 2a). For lower numbers of injected cells suspended in 1× PBS with 2% FBS, cells were trapped almost perfectly within the acoustic microstreaming at 6 V_{p-p} and 50.2 kHz and were not released to the outlets. As more cells were injected into the device, the acoustic microstreaming vortices gradually filled up to their capacities and became saturated, decreasing the overall capture efficiency from 99% to 94% (Fig. 2a and b). The number of captured cells within acoustic microstreaming linearly increased with the number of injected cells. The device demonstrated high capture efficiency and became saturated with around 230 000 injected cells for LCATs with 200 pairs of dead end side channels, averaging 1150 cells per pair of dead end side channels. Captured cells remain stable within the acoustic microstreaming, making this device well suited for rare cell capture application from large volumes of blood samples. We then determined the number of pairs of dead end side channels required to capture 16 µm cells from whole blood

assuming 1% of the whole blood contains 16 µm cells or

larger, including leukocytes, CTCs and cCAFs, and found that approximately 327 pairs of dead end side channels are necessary for device to process 7.5 mL of patient blood and maintain below saturation of the acoustic microstreaming (Fig. 2c and d). 29,31,44 Experiments with 230 000 cells were again performed for LCATs channels that were 750 μm in width at 6 V_{p-p} and 50.2 kHz and showed near perfect trapping.

Demonstration of high-throughput cell capture from blood samples

In this work, we preprocessed whole blood with RBC lysis buffer to remove most of the RBCs before LCATs separation. It is worth noting that the microbubble stability is highly dependent on the fluid viscosity and suspension of cells in the saline buffer greatly decreases fluid viscosity and enhances the stability of microbubble and the duration of the experiments from approximately 5 minutes to 30 minutes (Fig. S4 and S5†). Similar microfluidic techniques also reported no significant damages to isolated WBCs or CTCs using RBC lysis buffer. ^{30,31} After incubating 7.5 mL of healthy donor blood with ammonium–chloride–potassium (ACK) lysis

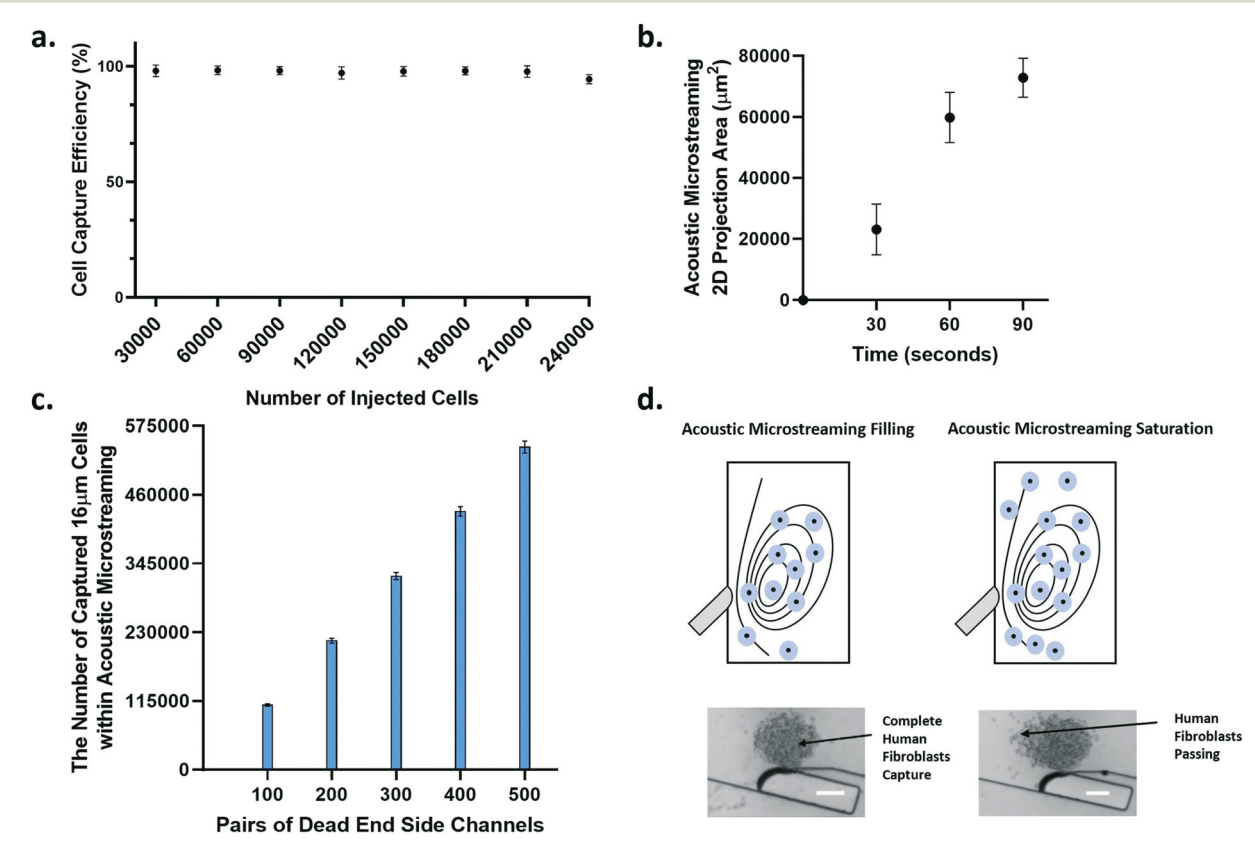


Fig. 2 LCATs characteristics. a) The capture efficiency as a function of the number of cells being injected (N = 3). b) The acoustic microstreaming area within each device as a function of time (N = 3). c) The number of cells that are 16 μ m larger can be captured within acoustic microstreaming as a function of the number of pairs of dead end side channels (N = 3). d) Schematic describing acoustic microstreaming filling and saturation and example image of trapped human lung fibroblasts inside acoustic microstreaming. Scale bar: 100 μ m.

serpentine design with 6 columns and each column contained 15 cavity pairs, so we designed four LCATs in parallel with 90 pairs of dead end side channels for a total of 360 pairs of dead end side channels and one shared inlet reservoir so that pumping rate increased by nearly four-fold from $8.9~\mu L~min^{-1}$ to $29.6~\mu L~min^{-1}$ (Fig. 3a-ii). In addition, we added 44 more pairs of dead end side channels to fully cover the surface of the piezoelectric transducer to absorb as much bulk acoustic wave as possible while maintaining the same number of columns to reduce channel resistance. We also smoothened the device inlet geometry to produce gentle flow and further obtained two-fold increase of pumping rate from 29.6 $\mu L~min^{-1}$ to 70.4 $\mu L~min^{-1}$ (Fig. 3b-i and S7†).

buffer (Biolegend, USA), pellets consisting of WBCs, CTCs and cCAFs were prepared via centrifugation (Fig. S6†). These pellets were then mixed with 500 μ L of PBS saline buffer and injected into the device (750 μ m in width) at 50 μ L per injection. Since there was still considerate number of RBCs remaining after RBC lysis treatment of whole blood (80% of the RBC lysed solution was RBCs), LCATs allowed further purification of smaller RBCs and resulted in ultrahigh enriched WBCs sample with enrichment ratio of 5733 (Fig. 3a-i and Video S1†). To ensure LCATs have enough pairs of dead end side channels (minimum of 327) and also enhance the throughput of the LCATs, we first employed a parallel multi-channel design to increase the number of cavity pairs. The LCATs with 90 cavity pairs had

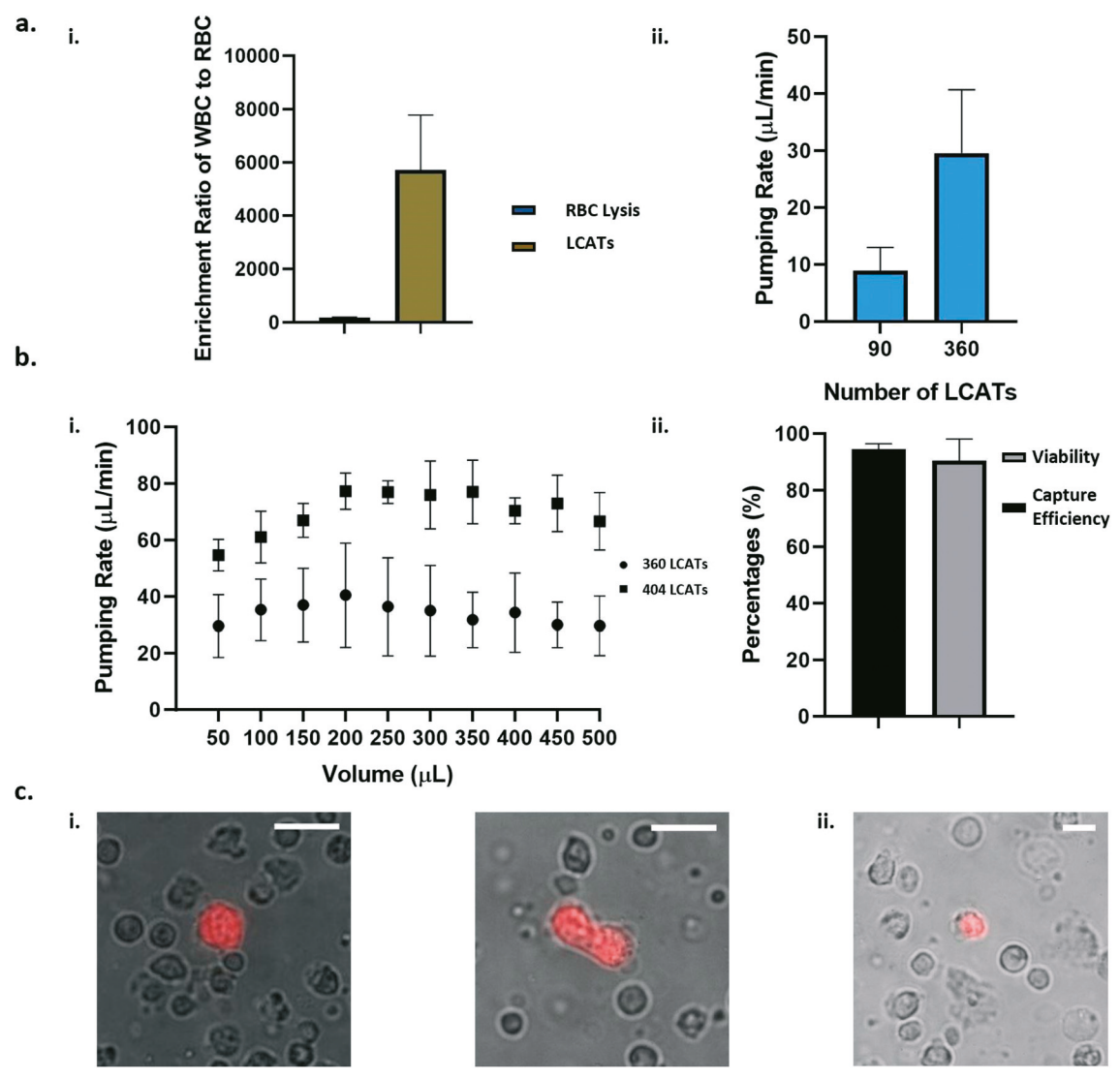


Fig. 3 High throughput device pumping rate and rare cell capture efficiency. a) Multiplexed LCATs can increase pumping rate by four-fold. (i) Highly enriched sample collected from LCATs compared with RBC lysed blood sample (N = 3). (ii) Pumping rate comparison between LCATs with 90 and 360 pairs of dead end side channels (N = 3). b) Further improvement of multiplexed LCATs to fully occupy the space of acoustic transducers. (i) Pumping rate between two different multiplexed LCATs (N = 3). (ii). Capture efficiency of spiked human lung fibroblasts and viability of trapped blood cells (N = 3). c) Captured normal human lung fibroblasts collected from devices. (i) Example image of human lung fibroblasts under 40×0 objective lense. (ii) Example image of human lung fibroblasts under 20×0 objective lense. Scale bar: $20 \mu m$.

Lab on a Chip

We then validated the rare cell capture performance from 7.5 mL of healthy donor blood. The WBCs concentration ranged from 4-6 million per mL of blood. To investigate rare cell trapping efficiency, 100 to 300 fibroblasts were stained with red cell tracker dye to distinguish between blood cells and then spiked into 7.5 mL of lysed blood samples under the same operational condition described above. Cells were collected from the two collection outlets and the fluorescence stained fibroblasts were counted on cell countess slides, and rare cell capture efficiency was determined by dividing the total number of captured cells by the total number of spiked cells (Materials and methods). The capture efficiency of 94% was obtained from all repeated experiments with the lowest repeat being 92.82% and the viability of trapped cells within acoustic microstreaming was 90% (Fig. 3b-ii and c and Table S1†). For multiplexed LCATs design with 404 pairs of dead end side channels, the device achieved processing time within 8 minutes from 7.5 mL of healthy donor blood (-Fig. 3b-i and Video S2†).

Isolation of CTCs and cCAFs from breast cancer patients across different stages

After device validation and demonstration of rare cell capture from healthy donor blood samples, we performed CTCs and cCAFs separation using blood samples that were collected from breast cancer patients across different cancer stages.

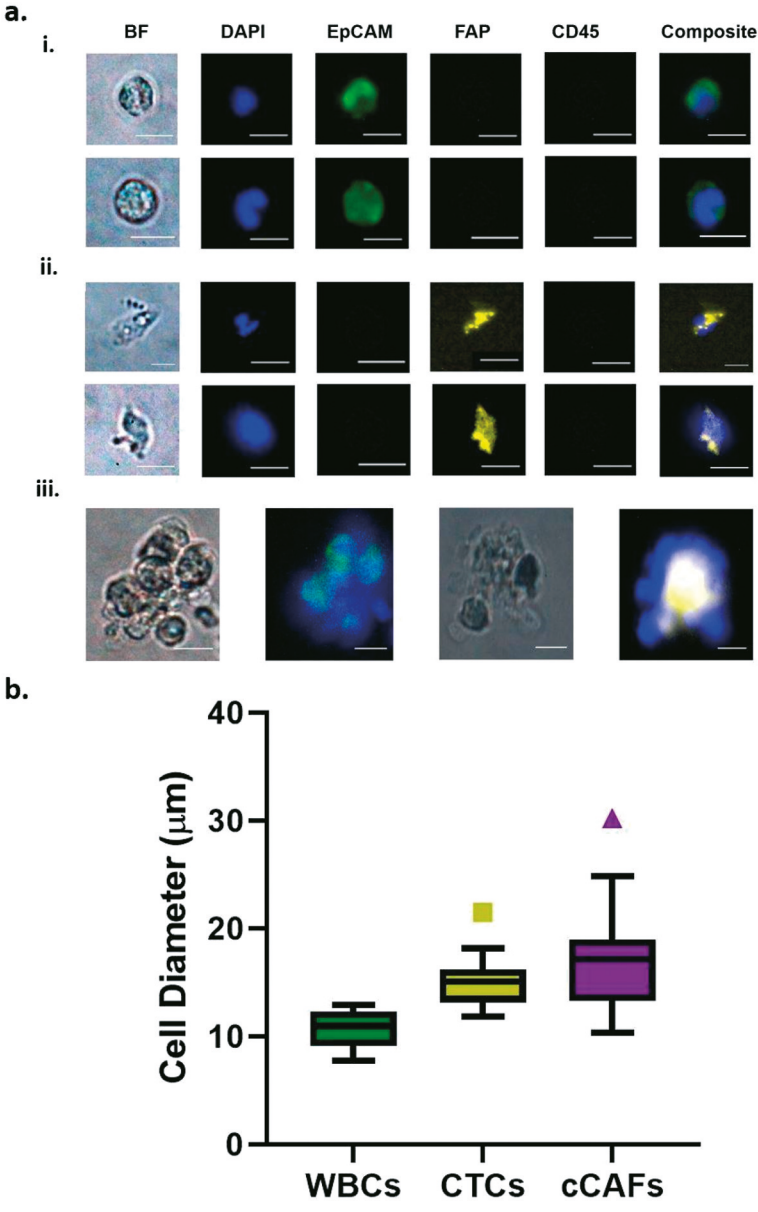


Fig. 4 Collection of CTCs and cCAFs from breast cancer patients. a) Example fluorescent images of collected cells. (i) Immunostaining images of CTCs. Scale bar: 10 µm. (iii) Immunostaining images of spindle-shaped cCAFs. Scale bar: 10 µm. (iii) Immunostaining images of CTCs and cCAFs clusters. Scale bar: 10 μ m. b) Size distribution of collected CTCs, cCAFs and WBCs (N=45).

One of the key phenotypic features of the CTCs and cCAFs is their larger sizes compared with the sizes of immune cells and RBCs. We further analyzed the size distribution of CTCs, cCAFs and WBCs. The mean diameters of CTCs, cCAFs and WBCs were 15.02 μ m, 17.28 μ m, and 10.75 μ m. The upper 50% of the size distribution ranged from 15 to 21.5 μ m for CTCs, 17 to 30 μ m for cCAFs, and 11 to 12.9 μ m for WBCs (Fig. 4b). The size distribution of CTCs and cCAFs between WBCs all presented a p-value of less than 0.05.

Based on the fluorescent immunostaining criteria, we identified CTCs from seven metastatic breast cancer patients, two nonmetastatic locoregional breast cancer patients but none from healthy donors (Fig. 4a-i). We also identified cCAFs from five metastatic breast cancer patients, two nonmetastatic locoregional breast cancer patients and none from healthy donor (Fig. 4a-ii). CTC counts ranged from 1.5 to 347 per 7.5 mL of blood and cCAF counts ranged from 4 to 264 per 7.5 mL of blood from metastatic breast cancer patients. Furthermore, we identified CTC and cCAF clusters from two of the metastatic breast cancer patients (Fig. 4a-iii and Table S2†). We did not find any CTC or cCAF clusters from nonmetastatic locoregional breast cancer patients, suggesting that CTC or cCAF clusters likely facilitated the growth of metastasis.

Importantly, not all cCAFs presented circular shapes like CTCs. Although majority of the cCAFs presented circular shapes, we observed spindle shaped cCAFs that are a key feature of cancer associated fibroblast morphology, thus further confirming the presence of cancer associated fibroblast in patient peripheral blood circulation (Fig. 4a-ii).

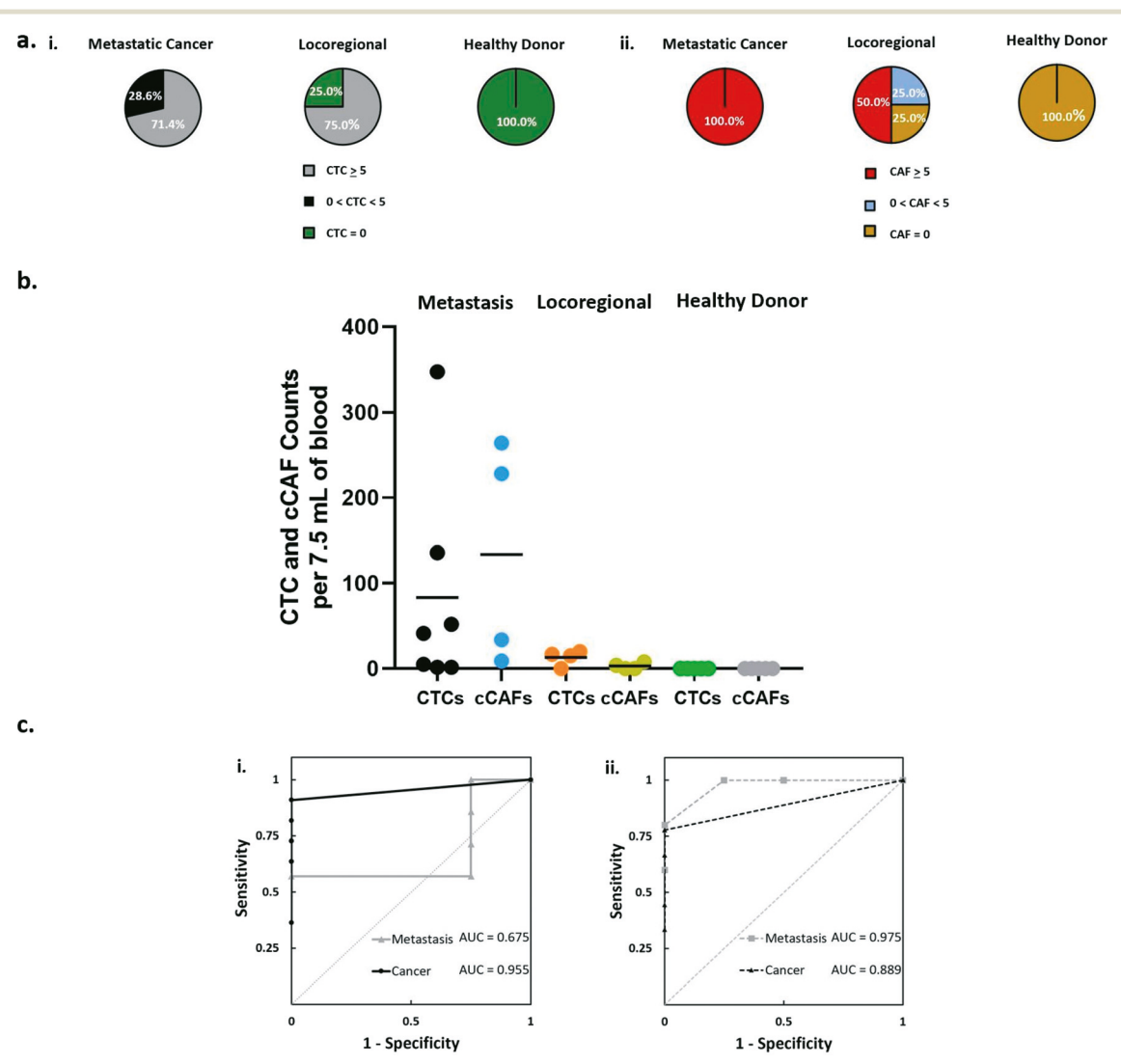


Fig. 5 CTCs and cCAFs are collected from eight metastatic breast cancer patients, four nonmetastatic locoregional breast cancer patients and five healthy donors. a) (i) CTCs percentages from metastatic breast cancer patients, nonmetastatic locoregional breast cancer patients and healthy donors. (ii) cCAFs percentages from metastatic breast cancer patients, nonmetastatic locoregional breast cancer patients and healthy donors. b) Cell counts for each patient across different disease states. c) ROC curves for (i) CTC and (ii) cCAF to evaluate cancer diagnostic accuracy.

Lab on a Chip **Paper**

Both CTCs and cCAFs also contained relatively smaller cells that overlapped with the size of WBCs.

We categorized CTC and cCAF counts into different cancer stages and healthy donor control. CTC counts from metastatic breast cancer patients were significantly higher than those of nonmetastatic locoregional breast cancer patients: the mean number of CTCs in metastatic breast cancer patients was 83.5 while the mean number of CTCs in nonmetastatic locoregional breast cancer patients was 13. cCAF counts also followed the same trend and showed elevated counts among metastatic breast cancer patients: the mean number of cCAFs in metastatic patients was 111.9 while the mean number of cCAFs in nonmetastatic locoregional cancer patients was 3 (Fig. 5a and b). Both CTCs and cCAFs had zero counts from healthy donors.

We also assessed the diagnostic performance of CTC and cCAF by building receiver operating characteristic (ROC) curves and evaluated the area under each curve. An AUC-ROC of 1 indicates a perfect discrimination of a test, whereas a lower AUC-ROC suggests a less reliable discrimination. The AUC-ROC for CTC counts distinguishing between advanced breast cancer patients and healthy individuals was 0.955, and the AUC-ROC for cCAF counts in distinguishing between advanced breast cancer patients and healthy individuals was 0.889. This suggested that CTCs outcompetes cCAFs in predicting advanced cancer and serving as a better early cancer detection biomarker (Fig. 5c).

Importantly, the AUC-ROC for CTC counts in distinguishing between metastatic breast cancer patients and nonmetastatic locoregional breast cancer patients decreased dramatically to 0.675, similar to reports using CTCs as a metastasis prediction biomarker. 45,46 However, the AUC-ROC for cCAF counts in distinguishing between metastatic breast cancer patients and nonmetastatic locoregional breast cancer patients increased from 0.889 to 0.975 (Fig. 5c). The poor diagnosis performance of CTCs in predicting metastasis could be caused by several factors: (a) false negativity from detecting CTCs that were undergoing epithelial to mesenchymal transition among more advanced cancer patients. (b) The elimination of CTCs from metastatic patients who were receiving aggressive treatment such as chemotherapy.⁴⁵ This further highlighted the clinical significance of cCAF as a better diagnostic marker for the prediction of breast cancer metastasis.

Interestingly, small portions of cCAFs were identified with smooth muscle actin known as α-SMA (Fig. S8†). The expression of α-SMA positivity in the cCAFs from breast cancer metastatic patients reflected their heterogeneities.⁴⁷ This result also indicated that FAP based immunostaining along with FAP targeted cell therapies could have missed some circulating cancer associated fibroblasts and led to incorrect cancer diagnosis. Although α-SMA is typically not considered due to inconsistent expression, they can be used to further understand the heterogeneity of cCAFs along with other fibroblast biomarkers such as vimentin.

Functional immune assessment from metastatic and nonmetastatic locoregional breast cancer patients

We also investigated whether there were differences in primary immune cells between nonmetastatic locoregional and metastatic cancers as increased metastasis is expected to cause immune suppression. By immunostaining innate immune cells, it was determined that there was no significant difference in terms of inflammatory monocytes (CD14⁺ and CD16⁺) and classical monocytes (CD14⁺ and CD16⁻) between metastatic and nonmetastatic locoregional cancer patients (Fig. S9a†). Similarly, the proportions of dendritic cells were also compared between the two cancer stages: expression of the activation markers, CD86 and HLADR on these subsets did not show significant differences between nonmetastatic locoregional and metastatic breast cancer patients (Fig. S9b†).

To further investigate the suppression of the human immune system, we assessed the proportions and phenotypes of CD4⁺ and CD8⁺ T cells from the peripheral blood mononuclear cells (PBMCs). The expression of T cell exhaustion marker, programmed cell death protein 1 (PD-1) was evaluated on CD4⁺ and CD8⁺ T cells. There was a significant increase in the percentage of CD8⁺ T cells expressing the PD1 biomarker in metastatic breast cancer patients versus nonmetastatic locoregional breast cancer patients (Fig. 6a) while the level was comparable in CD4⁺ T cells (Fig. 6b). In the CD4⁺ compartment, however, there was a significant increase in the percentage of CD4 T cells expressing the regulatory T cell markers (CD4+, CD25high, CD127^{low}) in metastatic cancer patients compared to nonmetastatic locoregional breast cancer patients (Fig. 6c).

Discussion

The prognostic value of CTCs has been actively explored over the past decades and efforts at capturing and analyzing them provide valuable assessment and guidance for cancer diagnosis. 2,5,22,25,29,31 However, using CTCs as the only clinically significant biomarker has had mixed success in terms of improving patient overall survival rate and the falsenegativity of the detection method limits its wider adoption among clinics. 4,7,23,45,48 CAFs are a major component of the tumor microenvironment and have been shown to play a crucial role in signaling metastasis at distant organ sites.^{3,4,11,14,15,17,47,49} More importantly, evidence of cCAFs in the metastatic cancer patients' blood stream suggests the possibility of using cCAFs as a metastatic biomarker. A labelfree collection of rare circulating cells and a systematic study to understand tumor invasiveness as well as immune dysregulation under cancer metastasis is extremely valuable for disease prediction and identifying therapeutic regimes.

In this work, we have developed a multiplexed LCATs acoustic microstreaming platform for the simultaneous separation of CTCs, cCAFs and circulating immune cells in a high-throughput manner. With this platform we achieved rare-cell capture efficiency of 94% while maintaining

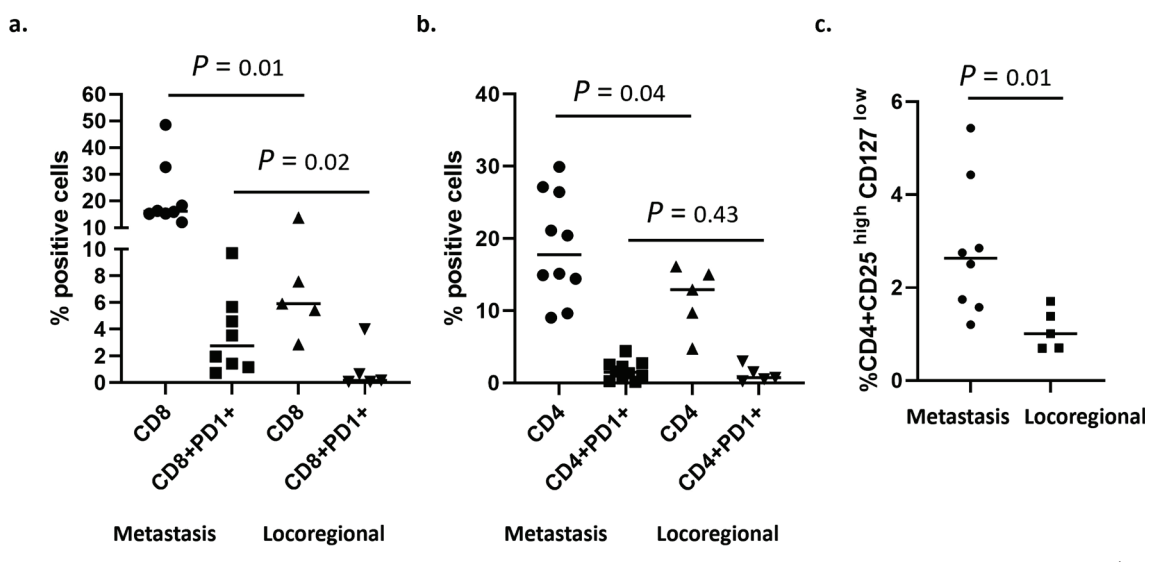


Fig. 6 Immune system evaluation from metastatic and nonmetastatic locoregional breast cancer patients. a) The increase in CD8 $^+$ T cell surface marker expressions in metastatic breast cancer patients compared with those of nonmetastatic locoregional breast cancer patients. b) The increase in CD4 $^+$ T cell surface marker expressions from nonmetastatic locoregional to metastatic breast cancer patients. c) The increase in regulatory cell markers from nonmetastatic locoregional to metastatic breast cancer patients. Group comparison is conducted by one-way ANOVA and a value of P < 0.05 is considered statistically different.

processing time within 8 minutes and demonstrated successful isolation of both CTCs and cCAFs from different stages of breast cancer patients, enabling clinicians to predict the likelihood of cancer metastasis. Upon successful capture of CTCs and cCAFs from blood samples, we assessed the diagnostic performance in discriminating between metastatic breast cancer patients, nonmetastatic locoregional breast cancer patients and healthy donors. The CTC test showed a significant diagnostic performance to predict the absence or presence of advanced cancer (AUC-ROC, 0.955), whereas cCAFs showed an excellent diagnostic performance to predict the occurrence of metastasis (AUC-ROC, 0.975). In addition, this work also allows us to reveal the heterogeneity of cCAFs and the therapeutic potential of targeting CTCs and cCAFs for cancer treatment. We demonstrated the heterogeneity of α-SMA expression in cCAFs from metastatic breast cancer patients. α-SMA in cCAFs has been previously identified in the context of cCAF subpopulations and biomarker development, and our work supports these findings. Better understanding of cCAFs heterogeneity enhances the resolution of cCAFs population and opens the possibility for precision targeting of cCAFs. More experimental and clinical studies are needed before the cCAFs can be used in clinical practice for decision making of cancer therapy. With the high efficiency capture of CTCs and cCAFs, further efforts to establish culturing CTC and cCAF cell lines would benefit the development of cancer therapy.⁵⁰ Having both cell populations in culturing assays and cell-cell pairing microfluidic devices would also enable the discovery of molecular signaling pathways to understand the role of tumor microenvironment involved in metastasis.51-53

Our platform also enabled collection of immune cells that would be useful to analyze effectiveness of CAR-T therapy and immunological pathways.⁵⁴ Another enormous advantage of this LCATs platform is in its ability to simultaneously pump and trap targeted cells within the acoustic microstreaming vortices. This presented tremendous flexibility to apply in situ antibody immunostaining within minutes instead of off-chip benchtop immunostaining that could take several hours (Fig. S10†). The flow cytometry data suggested that metastatic breast cancer patients' adaptive immune systems were compromised in comparison to nonmetastatic locoregional breast cancer patients. Metastatic breast cancer patients had significantly higher CD8⁺ cytotoxic T cells, but these may be immunosuppressive due to higher expression of PD-1 in CD8⁺ T cells. This suggested that the immune systems of the breast cancer patients were becoming significantly exhausted and losing effector functions against cancer cells. The number of T regulatory cells increased by approximately three-fold from nonmetastatic locoregional breast cancer to metastatic breast cancer, further suggesting suppression of the immune system. Interestingly, the number of T helper cells also increased by nearly two-fold from nonmetastatic locoregional breast cancer to metastatic breast cancer. CD4⁺ T helper cells are essential for the immune system to kill infected cells and contribute to maturation of CD8⁺ T cells and thus the elevated population of CD4⁺ T helper cells suggested a positive signal of immune system defense against cancer. However, induced T regulatory cells can also mature from CD4⁺ T cells under various mechanisms, indicating a dynamic immune response transitioning from positive regulation to suppression of the adaptive immune system. 55,56 Although subpopulation of monocytes have been reported to differentiate into tumor associated macrophages and promote tumor progression, we did not observe significance differences between the number

of classical monocytes and inflammatory monocytes in metastatic breast cancer patients and those of nonmetastatic locoregional breast cancer patients, 57-60 suggesting the role of monocytes lies heavily on the secreted proteins and other functional phenotypes rather than cell counts. The immunological T cell responses described here enable its potential clinical integration to use immune cell functional analysis as biomarkers to understand disease progression.⁶¹ Future work involves single cell analysis such as fluorescence in situ hybridization (FISH), profiling of metabolic activity and single cell RNA sequencing on multiple types of cells from patients. 62,63 We believe that the direction of this work also represents an important step towards advancing our understanding of human immune response in relation to cancer. These data have the potential to uncover relationships between subtypes of tumor microenvironment and tumor cells that have not been revealed with existing miniaturized systems.64

Conclusion

Overall, this work demonstrates for the first time, a liquid biopsy approach for rapid isolation and enrichment of multiple types of circulating rare cells and circulating immune cells within 8 minutes without compromising cell viability. The metastatic diagnosis accuracy of cCAFs outperformed the diagnostic accuracy of CTCs and quantitative measurement of primary T cell exhaustion could lead to the development of a new cancer metastatic test. The development of the integrated strategies will continue to expand current understanding of cellular phenotypes and their functions in the immune system. Further study that involves a larger patient cohort will increase the accuracy of cCAFs and its clinical utility in establishing a new paradigm to understand metastasis for the development of advanced cancer diagnostic tests and anti-metastasis drugs.

Author contribution

R. J., R. P., A. A. and A. P. L. designed experiments. R. J. conducted microfluidic device design validation, characterization, and investigation; S. A. performed flow cytometry analysis. M. A. performed numerical simulation. R. J. wrote the manuscript. A. P. L. supervised and edited the manuscripts.

Conflicts of interest

The authors declare no conflict of interest.

Acknowledgements

The authors would like to thank Yu-Hsi Chen, Paul B. Yoo and Dr. Xuan Li for helpful discussions and advice on experimental design. The authors thank nurses, doctors, and training staff from the Chao Family Comprehensive Cancer Center for their help in obtaining blood samples from breast cancer patients.

This work was supported by the American Cancer Society Institutional Research Grant (IRG-19-145-16) and partially by the National Science Foundation and the industrial members of the Center for Advanced Design and Manufacturing of Integrated Microfluidics (NSF I/UCRC award number IIP 1841509).

References

- B. Jundi, H. Ryu, D.-H. Lee, R.-E. E. Abdulnour, B. D. Engstrom, M. G. Duvall, A. Higuera, M. Pinilla-Vera, M. E. Benson, J. Lee, N. Krishnamoorthy, R. M. Baron, J. Han, J. Voldman and B. D. Levy, *Nat. Biomed. Eng.*, 2019, 3, 961–973.
- 2 R. L. Siegel, K. D. Miller and A. Jemal, Ca-Cancer J. Clin., 2018, 68, 7–30.
- 3 P. S. Steeg, Nat. Rev. Cancer, 2016, 16, 201-218.
- 4 Z. Ao, S. H. Shah, L. M. Machlin, R. Parajuli, P. C. Miller, S. Rawal, A. J. Williams, R. J. Cote, M. E. Lippman, R. H. Datar and D. El-Ashry, *Cancer Res.*, 2015, 75, 4681–4687.
- 5 J. Che, V. Yu, E. B. Garon, J. W. Goldman and D. Di Carlo, Lab Chip, 2017, 17, 1452–1461.
- 6 X. Zhang, L. Wei, J. Li, J. Zheng, S. Zhang and J. Zhou, *Mol. Med. Rep.*, 2019, 19, 601–608.
- 7 M. Dhar, J. N. Lam, T. Walser, S. M. Dubinett, M. B. Rettig and D. Di Carlo, *Proc. Natl. Acad. Sci. U. S. A.*, 2018, 115, 9986–9991.
- 8 M. Labib, Z. Wang, S. U. Ahmed, R. M. Mohamadi, B. Duong, B. Green, E. H. Sargent and S. O. Kelley, *Nat. Biomed. Eng.*, 2020, DOI: 10.1038/s41551-020-0590-1.
- 9 J.-C. Marine, S.-J. Dawson and M. A. Dawson, *Nat. Rev. Cancer*, 2020, 20, 743–756.
- 10 Y.-H. Cheng, Y.-C. Chen, E. Lin, R. Brien, S. Jung, Y.-T. Chen, W. Lee, Z. Hao, S. Sahoo, H. Min Kang, J. Cong, M. Burness, S. Nagrath, M. S. Wicha and E. Yoon, *Nat. Commun.*, 2019, 10, 2163.
- 11 D. F. Quail and J. A. Joyce, Nat. Med., 2013, 19, 1423-1437.
- 12 H. Peinado, H. Zhang, I. R. Matei, B. Costa-Silva, A. Hoshino, G. Rodrigues, B. Psaila, R. N. Kaplan, J. F. Bromberg, Y. Kang, M. J. Bissell, T. R. Cox, A. J. Giaccia, J. T. Erler, S. Hiratsuka, C. M. Ghajar and D. Lyden, *Nat. Rev. Cancer*, 2017, 17, 302–317.
- 13 X. Y. Li, M. Dong, X. Y. Zang, M. Y. Li, J. Y. Zhou, J. J. Ma and G. Y. Wang, *Am. J. Transl. Res.*, 2020, 12, 332–342.
- 14 S. Chen, A. Giannakou, S. Wyman, J. Gruzas, J. Golas, W. Zhong, C. Loreth, L. Sridharan, T.-T. Yamin, M. Damelin and K. G. Geles, *Proc. Natl. Acad. Sci. U. S. A.*, 2018, 115, E11671–E11680.
- 15 A. Orimo, P. B. Gupta, D. C. Sgroi, F. Arenzana-Seisdedos, T. Delaunay, R. Naeem, V. J. Carey, A. L. Richardson and R. A. Weinberg, *Cell*, 2005, 121, 335–348.
- 16 E. Puré and R. Blomberg, Oncogene, 2018, 37, 4343-4357.
- 17 A. D. Rhim, P. E. Oberstein, D. H. Thomas, E. T. Mirek, C. F. Palermo, S. A. Sastra, E. N. Dekleva, T. Saunders, C. P. Becerra, I. W. Tattersall, C. B. Westphalen, J. Kitajewski, M. G. Fernandez-Barrena, M. E. Fernandez-Zapico, C. Iacobuzio-Donahue, K. P. Olive and B. Z. Stanger, Cancer Cell, 2014, 25, 735–747.

Paper

- 18 A. Satelli, I. Batth, Z. Brownlee, A. Mitra, S. Zhou, H. Noh, C. R. Rojas, H. Li, Q. H. Meng and S. Li, *Oncotarget*, 2017, 8, 49329–49337.
- 19 M. L. Jones, J. Siddiqui, K. J. Pienta and R. H. Getzenberg, *Prostate*, 2013, 73, 176–181.
- 20 A. Agarwal, M. Balic, D. El-Ashry and R. J. Cote, *Cancer J.*, 2018, 24, 70–77.
- 21 G. J. Koelwyn, X. Zhuang, T. Tammela, A. Schietinger and L. W. Jones, *Nat. Metab.*, 2020, 2, 849–857.
- 22 O. Nordgård, K. Tjensvoll, B. Gilje and K. Søreide, *Br. J. Surg.*, 2018, **105**, e110–e120.
- 23 C. L. Yankaskas, K. N. Thompson, C. D. Paul, M. I. Vitolo, P. Mistriotis, A. Mahendra, V. K. Bajpai, D. J. Shea, K. M. Manto, A. C. Chai, N. Varadarajan, A. Kontrogianni-Konstantopoulos, S. S. Martin and K. Konstantopoulos, *Nat. Biomed. Eng.*, 2019, 3, 452–465.
- 24 C. Alix-Panabières and K. Pantel, Cancer Discovery, 2016, 6, 479–491.
- 25 G. Galletti, L. Portella, S. T. Tagawa, B. J. Kirby, P. Giannakakou and D. M. Nanus, *Mol. Diagn. Ther.*, 2014, **18**, 389–402.
- 26 J.-Y. Pierga, F.-C. Bidard, C. Mathiot, E. Brain, S. Delaloge, S. Giachetti, P. de Cremoux, R. Salmon, A. Vincent-Salomon and M. Marty, *Clin. Cancer Res.*, 2008, 14, 7004–7010.
- 27 D. R. Gossett, W. M. Weaver, A. J. Mach, S. C. Hur, H. T. K. Tse, W. Lee, H. Amini and D. Di Carlo, *Anal. Bioanal. Chem.*, 2010, 397, 3249–3267.
- 28 J. Zhang, S. Yan, D. Yuan, G. Alici, N.-T. Nguyen, M. Ebrahimi Warkiani and W. Li, *Lab Chip*, 2016, **16**, 10–34.
- 29 E. Sollier, D. E. Go, J. Che, D. R. Gossett, S. O'Byrne, W. M. Weaver, N. Kummer, M. Rettig, J. Goldman, N. Nickols, S. McCloskey, R. P. Kulkarni and D. Di Carlo, *Lab Chip*, 2014, 14, 63–77.
- 30 M. E. Warkiani, G. Guan, K. B. Luan, W. C. Lee, A. A. S. Bhagat, P. Kant Chaudhuri, D. S.-W. Tan, W. T. Lim, S. C. Lee, P. C. Y. Chen, C. T. Lim and J. Han, *Lab Chip*, 2014, 14, 128–137.
- 31 M. Wu, P.-H. Huang, R. Zhang, Z. Mao, C. Chen, G. Kemeny, P. Li, A. V. Lee, R. Gyanchandani, A. J. Armstrong, M. Dao, S. Suresh and T. J. Huang, *Small*, 2018, 14, 1801131.
- 32 P. Li, Z. Mao, Z. Peng, L. Zhou, Y. Chen, P.-H. Huang, C. I. Truica, J. J. Drabick, W. S. El-Deiry, M. Dao, S. Suresh and T. J. Huang, *Proc. Natl. Acad. Sci. U. S. A.*, 2015, 112, 4970–4975.
- 33 M. Wu, A. Ozcelik, J. Rufo, Z. Wang, R. Fang and T. Jun Huang, *Microsyst. Nanoeng.*, 2019, 5, 32.
- 34 X. Hu, D. Zhu, M. Chen, K. Chen, H. Liu, W. Liu and Y. Yang, *Lab Chip*, 2019, **19**, 2549–2556.
- 35 I. F. Cheng, W.-L. Huang, T.-Y. Chen, C.-W. Liu, Y.-D. Lin and W.-C. Su, *Lab Chip*, 2015, 15, 2950–2959.
- 36 V. Narayanamurthy, Z. E. Jeroish, K. S. Bhuvaneshwari, P. Bayat, R. Premkumar, F. Samsuri and M. M. Yusoff, *RSC Adv.*, 2020, **10**, 11652–11680.
- 37 N. Garg, T. M. Westerhof, V. Liu, R. Liu, E. L. Nelson and A. P. Lee, *Microsyst. Nanoeng.*, 2018, 4, 17085.
- 38 M. V. Patel, A. R. Tovar and A. P. Lee, *Lab Chip*, 2012, **12**, 139–145.
- 39 A. R. Tovar and A. P. Lee, *Lab Chip*, 2009, **9**, 41–43.

- 40 M. V. Patel, I. A. Nanayakkara, M. G. Simon and A. P. Lee, Lab Chip, 2014, 14, 3860–3872.
- 41 A. R. Tovar, M. V. Patel and A. P. Lee, *Microfluid. Nanofluid.*, 2011, 10, 1269–1278.
- 42 P. Marmottant and S. Hilgenfeldt, *Nature*, 2003, **423**, 153–156.
- 43 P. Marmottant and S. Hilgenfeldt, *Proc. Natl. Acad. Sci. U. S. A.*, 2004, **101**, 9523–9527.
- 44 M. Pødenphant, N. Ashley, K. Koprowska, K. U. Mir, M. Zalkovskij, B. Bilenberg, W. Bodmer, A. Kristensen and R. Marie, *Lab Chip*, 2015, 15, 4598-4606.
- 45 L. Jin, W. Zhao, J. Zhang, W. Chen, T. Xie, L. Wang, W. Fan, S. Xie, J. Shen, H. Zheng, W. Hu, Q. Wei, M. Dong, Q. Wang, J. Shen and Y. Liu, *Cancer Med.*, 2020, 9, 1638–1647.
- 46 F. Tanaka, K. Yoneda, N. Kondo, M. Hashimoto, T. Takuwa, S. Matsumoto, Y. Okumura, S. Rahman, N. Tsubota, T. Tsujimura, K. Kuribayashi, K. Fukuoka, T. Nakano and S. Hasegawa, Clin. Cancer Res., 2009, 15, 6980–6986.
- 47 M. Bartoschek, N. Oskolkov, M. Bocci, J. Lövrot, C. Larsson, M. Sommarin, C. D. Madsen, D. Lindgren, G. Pekar, G. Karlsson, M. Ringnér, J. Bergh, Å. Björklund and K. Pietras, *Nat. Commun.*, 2018, 9, 5150.
- 48 J. Ko, N. Bhagwat, S. S. Yee, T. Black, C. Redlinger, J. Romeo, M. O'Hara, A. Raj, E. L. Carpenter, B. Z. Stanger and D. Issadore, *Lab Chip*, 2017, 17, 3086–3096.
- 49 N. Ortiz-Otero, A. B. Clinch, J. Hope, W. Wang, C. A. Reinhart-King and M. R. King, *Oncotarget*, 2020, **11**, 1037–1050.
- 50 B. L. Khoo, G. Grenci, Y. B. Lim, S. C. Lee, J. Han and C. T. Lim, *Nat. Protoc.*, 2018, 13, 34–58.
- 51 B. Dura, M. M. Servos, R. M. Barry, H. L. Ploegh, S. K. Dougan and J. Voldman, *Proc. Natl. Acad. Sci. U. S. A.*, 2016, 113, E3599–E3608.
- 52 B. Dura, S. K. Dougan, M. Barisa, M. M. Hoehl, C. T. Lo, H. L. Ploegh and J. Voldman, *Nat. Commun.*, 2015, **6**, 5940.
- 53 A. M. Skelley, O. Kirak, H. Suh, R. Jaenisch and J. Voldman, *Nat. Methods*, 2009, **6**, 147–152.
- 54 C. Murray, H. Miwa, M. Dhar, D. E. Park, E. Pao, J. Martinez, S. Kaanumale, E. Loghin, J. Graf, K. Rhaddassi, W. W. Kwok, D. Hafler, C. Puleo and D. Di Carlo, *Lab Chip*, 2018, 18, 2396–2409.
- 55 W. Chen, W. Jin, N. Hardegen, K.-J. Lei, L. Li, N. Marinos, G. McGrady and S. M. Wahl, J. Exp. Med., 2003, 198, 1875–1886.
- 56 D. Haribhai, J. B. Williams, S. Jia, D. Nickerson, E. G. Schmitt, B. Edwards, J. Ziegelbauer, M. Yassai, S. H. Li, L. M. Relland, P. M. Wise, A. Chen, Y. Q. Zheng, P. M. Simpson, J. Gorski, N. H. Salzman, M. J. Hessner, T. A. Chatila and C. B. Williams, *Immunity*, 2011, 35, 109–122.
- 57 L. Cassetta and J. W. Pollard, Cell Res., 2016, 26, 3-4.
- 58 P. L. Graney, S. Ben-Shaul, S. Landau, A. Bajpai, B. Singh, J. Eager, A. Cohen, S. Levenberg and K. L. Spiller, *Sci. Adv.*, 2020, **6**, eaay6391.
- 59 C. E. Olingy, H. Q. Dinh and C. C. Hedrick, *J. Leukocyte Biol.*, 2019, **106**, 309–322.
- 60 P.-L. Loyher, P. Hamon, M. Laviron, A. Meghraoui-Kheddar, E. Goncalves, Z. Deng, S. Torstensson, N. Bercovici, C. Baudesson de Chanville, B. Combadière, F. Geissmann, A.

- Savina, C. Combadière and A. Boissonnas, *J. Exp. Med.*, 2018, 215, 2536–2553.
- 61 C. A. Egelston, C. Avalos, T. Y. Tu, D. L. Simons, G. Jimenez, J. Y. Jung, L. Melstrom, K. Margolin, J. H. Yim, L. Kruper, J. Mortimer and P. P. Lee, *Nat. Commun.*, 2018, 9, 4297.
- 62 A. Raj, P. van den Bogaard, S. A. Rifkin, A. van Oudenaarden and S. Tyagi, *Nat. Methods*, 2008, 5, 877–879.
- 63 J. Wan, G. Sun, J. Dicent, D. S. Patel and H. Lu, *Lab Chip*, 2020, 20, 266–273.
- 64 X. He, S. Memczak, J. Qu, J. C. I. Belmonte and G.-H. Liu, *Nat. Metab.*, 2020, 2, 293–302.